Photoelectrochemically-assisted biofuel cell constructed by redox complex and g-C3N4 coated MWCNT bioanode

Bekir Çakiroğlu, Jérôme Chauvin, Alan Le Goff, Karine Gorgy, Mahmut Özacar, Michael Holzinger

Photoelectrochemically-Assisted Biofuel Cell Constructed by Redox Complex and g-C_3N_4 Coated MWCNT Bioanode

Bekir Çakıroğlu[a,b], *Jérôme Chauvin*[a], *Alan Le Goff*[a,d], *Karine Gorgy*[a], *Mahmut Özacar*[b,c*], *Michael Holzinger*[a,d]*

[a]*Université Grenoble Alpes, DCM UMR 5250, F-38000, Grenoble, France*

[b]*Sakarya University, Biomedical, Magnetic and Semiconductor Materials Research Center (BIMAS-RC), 54187 Sakarya, Turkey*

[c]*Sakarya University, Science & Arts Faculty, Department of Chemistry, 54187 Sakarya, Turkey*

[d]*CNRS, DCM UMR 5250, F-38000, Grenoble, France*

*Corresponding Author. Tel.:+90 264 295 60 41; Fax:+90 264 295 59 50

E-mail address: mozacar@hotmail.com(M.Ozacar).

*Corresponding Author. Tel.: +33 (0)4.56.52.08.11; Fax: +33 (0)4.56.52.08.05

E-mail address: michael.holzinger@univ-grenoble-alpes.fr

ABSTRACT:

Herein, we report a membraneless glucose and air photoelectrochemical biofuel cell (PBFC) with a visible light assisted photobioanode. Flavin adenine dinucleotide dependent glucose dehydrogenase (FADGDH) was immobilized on the combined photobioanode for the visible light assisted glucose oxidation (GCE|MWCNT|g-C_3N_4|Ru-complex|FADGDH) with a quinone mediated electron transfer. Bilirubine oxidase (BOx) immobilized on MWCNT coated GCE (GCE|BOx) was used as the cathode with direct electron transfer (DET). An improvement of biocatalytic oxidation current was observed by 6.2% due in part to the light-driven electron-transfer. The large oxidation currents are probably owing to the good contacting of the immobilized enzymes with the electrode material and the utilization of light assisted process. Under the visible light, the photobioanode shows an anodic photocurrent of 1.95 μA cm^2 at attractively low potentials *viz.* -0.4 vs Ag/AgCl. The lower-lying conduction band of g-C_3N_4 as compared to Ru-complexes decreases the rate of hole and electron recombination and enhances the charge transportation. The bioanode shows maximum current density for glucose oxidation up to 6.78 μA cm^{-2} at 0.2 V vs Ag/AgCl at pH:7. The performance of three promising Ru-complexes differing in chemical and redox properties were compared as electron mediators for FADGDH. Upon illumination, the PBFC delivered a maximum power density of 28.5 ± 0.10 μW cm^{-2} at a cell voltage of +0.4 V with an open circuit voltage of 0.64 V.

KEYWORDS: Photoelectrochemical biofuel cell, Glucose bioelectrocatalysis, FADGDH, BOx, Ruthenium complexes, Photoelectrochemical biosensor

1. INTRODUCTION

Enzymatic Biofuel cells (BFCs) convert chemical energy directly into electricity under moderate operation conditions, *viz*. neutral pH and ambient temperature, from the oxidation of low-cost, and sustainable sources without membranes (Gross et al., 2017; Lalaoui et al., 2015; Milton et al., 2013; Monsalve et al., 2015; Rasmussen et al., 2016). Biofuel cells can be easily integrated into devices due to their merits of lightweight and can enable us to produce self-powered biosensors (Bourourou et al., 2014; Jeerapan et al., 2016). Nowadays, the studies on BFCs are focuced on the improvement of the power density, voltage output, and stability (Elouarzaki et al., 2016; Moehlenbrock and Minteer, 2008; Xiao et al., 2019). Also, glucose is widely used fuel owing to its higher energy per weight and availibility in biological fluids, which give rise to production of miniaturized BFCs (Gross et al., 2017; Xiao et al., 2019). Sunlight energy is an extremely abundant and renewable resource (delivering $3x10^{24}$ joules per year) available on earth and technologies such as photoelectrochemical (PEC) systems have been drawn to the efficient capture, conversion and storage of solar energy handled by custom-made semiconductor materials (Zhao et al., 2015). As such, sunlight harnessing is a powerful and encouraging options for power output enhancement in BFC performances(Wang et al., 2012; Yu et al., 2016b). The emerging photoelectrochemical BFCs (PBFCs) incorporate the aspects of both enzymatic biofuel cells and dye-sensitized solar cells and enable us to design light assisted biocatalysts with energy conversion from light and chemical energy to produce electricity (Yang et al., 2014; Yu et al., 2016b). However, the technology is still in its infancy and highly efficient semiconducting hybrid materials are needed without compromising electrical conductivity in order to realize its full potential (Zhao et al., 2015). In PEC systems, combination of different photosensitive materials diminishes the recombination processes and gives rise to a cascade of electron-transfer steps by increasing quantum efficiency (Çakıroğlu and Özacar, 2019, 2018; Zhao et al., 2015). PBFCs have been fabricated with efficient photon-to-current approaches to enhance the energy conversion efficiency(Yu et al., 2016a). g-C_3N_4 is a promising mid-wide bandgap semiconductor (2.7 eV; 460 nm wavelength) with its aromatic and periodic structure and requires sensitization to harness the visible light efficiently(Dong et al., 2016). In a recent study, a PBFC containing g-C_3N_4 displayed open-circuit voltages (V_{OC}) varying with the contact distance between the components, which enable us to measure the microRNA on a self-powered mode (Gai et al., 2020). Ruthenium and osmium polypyridinyl complexes have been used as mediators or photosensitizers in enzyme electrodes owing to their favorable oxidizing potential, which

suits thermodynamically enzyme catalyzed glucose oxidation and long excited state lifetimes(Fritea et al., 2019; Riedel et al., 2018). Therefore, coupling such complexes with semiconductors is a promising way for developing visible light-active PEC systems(Zhao et al., 2014). Favorable binding between the photosensitizer and semiconductors is needed to accomplish efficient electron transfer from the excited redox-complex to the semiconductor and eliminates the need for diffusing mediators(Kumar et al., 2017). Recently, flavin adenine dinucleotide dependent glucose dehydrogenase (FADGDH) has been emerged as a promising enzyme in bioanode fabrication owing to its high substatially and catalytic activity, oxygen independency and thus prevents the hydrogen peroxide release(Gross et al., 2017; Ross D Milton et al., 2015). However, FADGDH requires a mediator for the electron transfer, which is mainly based on redox complexes(Riedel et al., 2018). $[Ru(bpy)_3]^{2+}$- based redox complexes (bpy = 2,2'-bipyridine) are robust structures and have tunable effective band gaps which make them promising candidates for the optimization of PBFCs to achieve maximum efficiency(Reuillard et al., 2014). Multi-walled carbon nanotubes (MWCNTs) are superior to other advanced materials in bioelectrode production owing to their large surface area, satisfying stability and excellent conductivity and facilitate the immobilization of aromatic molecules by π-π interactions(Gross et al., 2018; Holzinger et al., 2012).

Herein, we report a PBFCs fabrication combining g-C_3N_4 and MWCNT along with three different types of Ru-complexes bearing 1, 2 or 3 quinone mediator ligands for the photobioanode construction. The objective is the development of efficient multicomponent semiconductor bioanode with high performance for enzyme wiring. The utilization of Ru-complex with a phenanthrolinequinone mediator ligand as an electron mediator for the fungus-derived FADGDH has led to the improved oxidation current. Ru-complexes anchored to g-C_3N_4 can act as the sensitizers and their energy levels match well with those of g-C_3N_4. Also, the porous structure of MWCNT allows stable and high enzyme and Ru-complex loading with fast mass transportation and intimate interfacial communication within architecture, which leads to efficient electron transfer between FADGDH and the electrode. This study highlights the efficient wiring of FADGDH to Ru-complex sensitized g-C_3N_4|MWCNT electrode material for the light-assisted glucose oxidation.

2. EXPERIMENTAL SECTION

The experimental details and electrochemical characterization of the complexes can be found in the supporting information.

3. RESULTS AND DISCUSSION

3.1. Structural Characterization and Electrochemical Features

Ru-complex-embedded MWCNT electrode was prepared by dropcoating the complexes onto the semiconductor-MWCNT coated electrode. The MWCNT functionalization is based on π–π stacking interactions between aromatic rings of g-C_3N_4 and PLQ, bipyridine and the 4,4′-bis(4-pyrenyl-1-ylbutyloxy)-2,2′- bipyridine) ligands of the Ru-complexes, which yields a stable composit (Akkaya et al., 2018; Gross et al., 2018). Three different types of Ru-complexes were synthesized (Scheme 1A) and Ru1 was used for the bioanode fabrication.

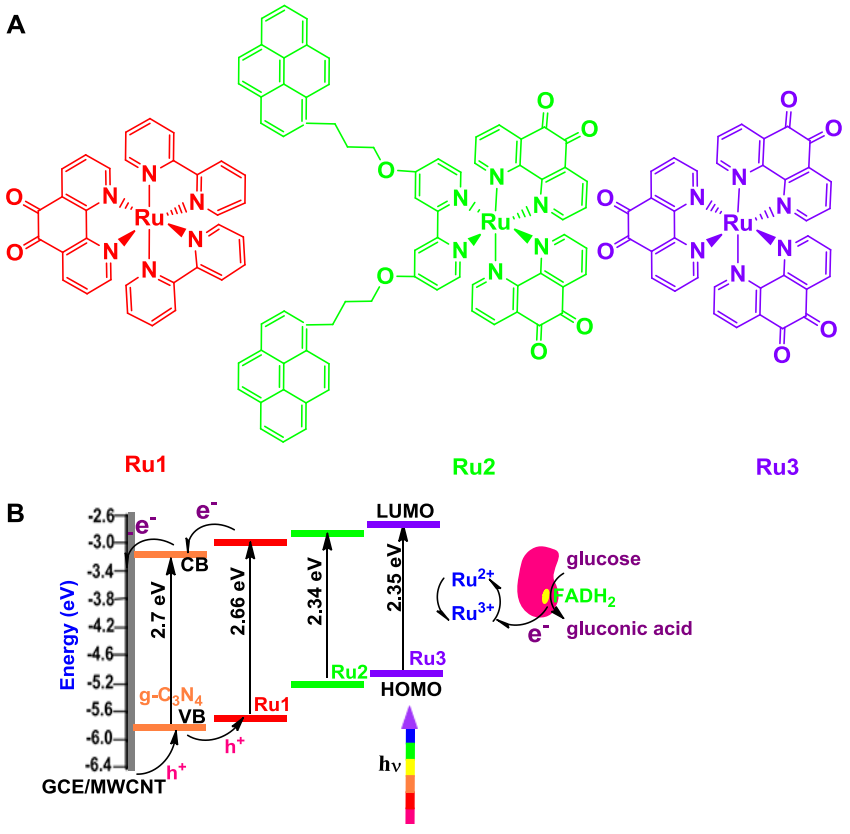

Scheme 1. Ru(II) complexes (counter ions: PF_6^-) (A); Schematic illustration of light-driven electron-transfer cascade with the energetic levels of photoactive materials (B).

The photograph and schematic illustration of PBFC assembly is given in Figure 1B and B, respectively. The photobioanode is made of three parts. The first part is the main photoactive material, viz. g-C_3N_4; the second part is a photoactive electron mediator (PLQ-Ru-complex),

and the third part is the biocatalyst (FADGDH). In the photoanode, the electrons from the enzymatic glucose oxidation are transferred from FADGDH to Ru-complex and then, to g-C_3N_4, and, finally, to the MWCNT coated GCE with a concomitant anodic photocurrent generation under irradiation (Scheme 1B). The fabricated electrodes are flat and reproducible. The SEM image of MWCNT displays the entangled network of MWCNTs forming a highly porous structure (Figure 1C). After the subsequent immobilization of g-C_3N_4 and the Ru-complex, a more compact topography compared to unmodified MWCNT can be identified but the porous morphology of the composite could be maintained(Figure 1D). The establishment of π–π stacking interactions between aromatic moieties of the Ru complexes, g-C_3N_4 and MWCNT lead to physisorption of photoactive materials on MWCNT coated electrodes and give rise to an efficient electron transfer through strongly interacted material. The surface was covered with Nafion to prevent the detachment of immobilized entities.

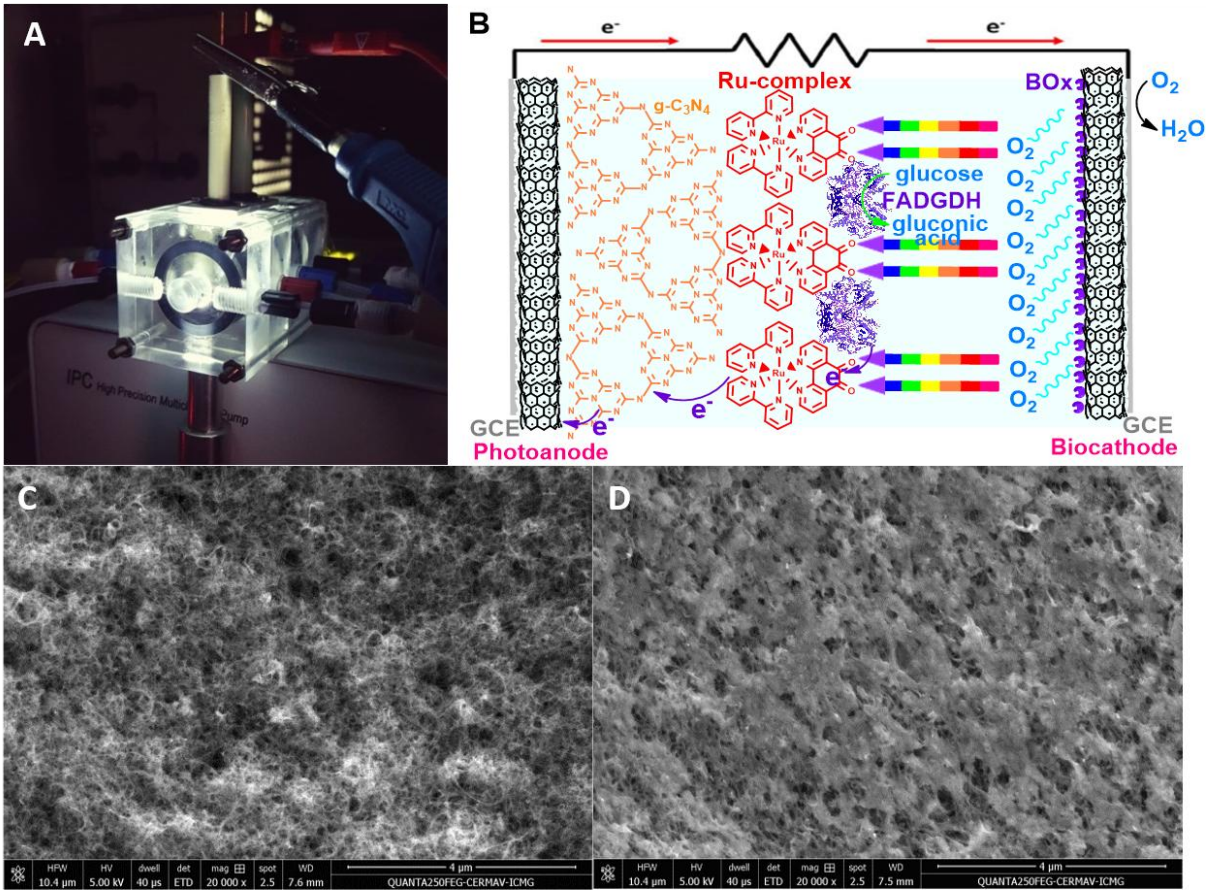

Figure 1. The photograph of PBFC during operation (A); the schematic illustration of the PBFC principle (B); SEM image of GCE|MWCNT (C) and GCE|MWCNT|g-C_3N_4|Ru complex (D)

In the optimal case, a monolayer of Ru-complexes in a good contact with g-C_3N_4 is adequate for photo-generated charge transfer and the high surface area of highly entangled nanotube

film contributes to the light harvesting. Additionally, MWCNTs collect the electrons efficiently coming from the semiconductor and improves the photocurrent generation(Gross et al., 2018).

The UV–visible spectra show the absorption bands recorded for all Ru-complexes in DMF (Figure 2A). Ru-complexes exhibit the typical metal-to-ligand-charge transfer transitions (MLCT) between 400 nm and 600 nm (Table 1) and the $\pi \rightarrow \pi^*$ transition of the ligand in the UV. Ru1 and Ru2 also reveal emissions properties confirming large Stokes shifts originated from the ^{3}MLCT excited state (Figure 2B, Table 1).

Figure S2, Figure S3.A and B show emission decay curves recorded for all Ru-complexes in DMF. The results indicate a clear diminishment of Ru1 excited state lifetime when associate with g-C_3N_4. The emission decay appear as monoexponential with partial quenching of the excited state occurs as evidenced by the decrease of the emission quantum yields (ϕ_L) and lifetimes (τ) of these complexes compared to regular $[Ru(bpy)_3]^{2+}$ (Caspar and Meyer, 1983)(For instance ϕ_L = 0.0024 vs 0.063 and τ = 179.4 vs. 912 ns for Ru1 relative to $[Ru(bpy)_3]^{2+}$*). The quenching process is more efficient when the number of quinone subunits increase around the Ru(II) center and Ru3 is almost not emissive as a consequence of a very efficient quenching process. This quenching process is due to an electron transfer reaction from the Ru(II)* center to the quinone acceptor units (Eswaran et al., 2014; Opperman et al., 1994). However via the cascade of electron transfer processes initiate by the oxidation of glucose, the Ru(II) complexes play the role of a redox mediator and will accept an electron from the $FADH_2$ on the PLQ ligand.

According to the Figure S2, in the anodic part, the CVs present a reversible oxidation at $E^{ox}_{1/2}$ = 1.09 V, corresponding to the metal-centered Ru^{III}/Ru^{II} redox system(Goss and Abruna, 1985). The reversible peaks at $E^{red}_{1/2}$ ($PLQ^{\cdot -}/PLQ$)= -0.48 V and $E^{red}_{1/2}$ ($PLQ^{2-}/PLQ^{\cdot -}$)= -1.26 V vs. $Ag/AgNO_3$ correspond to the two successive one-electron reduction of the PLQ ligand (Gross et al., 2017). $[Ru(PLQ)(bpy)_2]^{2+}$ displays two well-defined reversible peak systems at $E^{red}_{1/2}$ = -2.02, -1.82 vs. $Ag/AgNO_3$, which can be assigned to the ligand-centered reduction of bipyridine(Reuillard et al., 2014). The CV of $[Ru(PLQ)_2(pyrene)]^{2+}$ also reveals the irreversible oxidation of pyrene at onset of E^{ox} = 0.5 V by overlapping Ru (III)/(II) peak system(Reuillard et al., 2014). The CV of $[Ru(PLQ)_3]^{2+}$ shows two well-defined reversible peak systems at $E^{red}_{1/2}$= -0.61 and $E^{red}_{1/2}$= -0.89 V associated to the two successive one-electron reduction of the PLQ.

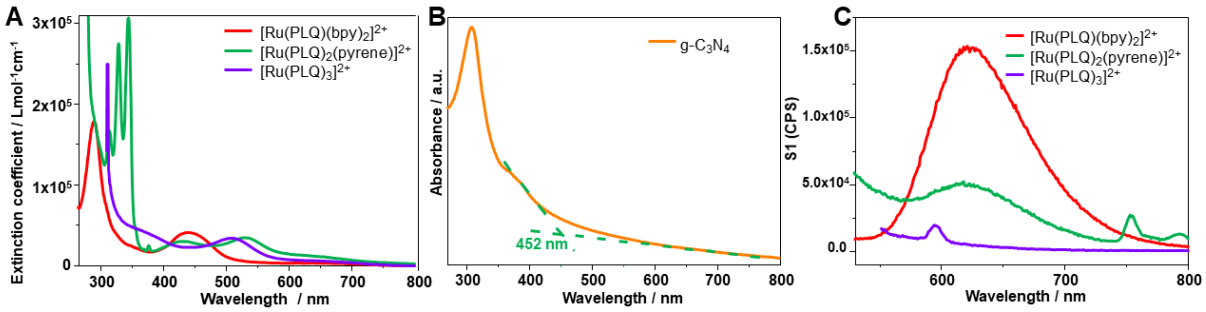

Figure 2. UV visible absorption spectra of g-C_3N_4 (orange curve), Ru1 (red curve), Ru2 (green curve), and Ru3 (purple curve) in DMF (B); The absorption spectrum of g-C_3N_4 (B); Fluorescence spectra of Ru1 (red curve), Ru2 (green curve), and Ru3 (purple curve) in DMF (C). (The concentration of Ru-complexes: 1.10^{-5} M)

We suppose that by irradiating the modified electrodes between 420 and 630 nm, the excited state of Ru (II) can be generated and further quenched by electron donor $FADH_2$. The incident photon-to-current conversion efficiency is enhanced by increasing molar extinction coefficient. Pyrene is a planar, symmetrical, electron-rich unit with an extended π-conjugated system(Elouarzaki et al., 2016). In the Ru2, the bipyridines have been functionalized with pyrenes in order to increase the complex loading efficiency on aromatic hybrid system(Cevallos-Vallejo et al., 2017).

The optical energy gap (E_g) of the g-C_3N_4 was determined by UV-vis absorbance spectra (Figure 2A inset). E_g was estimated as 2.74 eV by the cut-off wavelength of 452 nm, by using Eq. (1):

$$E_g\ (eV) = 1240/\lambda\ (cut-off)\ nm \qquad (1)$$

The energy levels of g-C_3N_4 were further surveyed using cyclic voltammetry according to bulk ionization potential (IP)(Zhang et al., 2018). Firstly, the $Ag/AgNO_3$ potential was calibrated by the oxidation potential of ferrocene (-4.80 eV vs vacuum), which was observed at 0 V, and the $Ag/AgNO_3$ potential was found to be -4.8 eV vs vacuum (Figure S4A). The valence band (VB) level (E_{VB}) of g-C_3N_4 was estimated as -5.90 eV using E_{ox} value of 1.10 V obtained from Figure S4B. Thus, E_{CB} was estimated as -3.16 eV using Eqs. (2) and (3):

$$E_{VB}\ (eV) = -IP = -\left(E_{ox} - I_{Ag/AgCl}\right) \qquad (2)$$

$$E_g(eV) = E_{CB} - E_{VB} \qquad (3)$$

Herein, E_{CB} is the CB energy, E_{ox} corresponds to the onset oxidation potential of g-C_3N_4, $I_{Ag/AgCl}$ equals to the absolute energy level of the reference electrode with respect to vacuum, and E_g is the band gap energy.

CV technique was performed to delve into the electrochemical behaviours of Ru-complexes in DMF (Figure S2.B, C and D). The CVs were recorded at a GCE in 1 mM solutions of ruthenium complexes in DMF containing supporting electrolyte 0.1 M $[Bu_4N]PF_6$ (scan rate: 0.1 $V.s^{-1}$). The highest occupied molecular orbital (HOMO), the lowest unoccupied molecular orbital (LUMO) energy levels and the E_g were estimated by the equations below:

$$E_{HOMO}(eV) = -e(E_{ox} + 4.80) \qquad (4)$$

$$E_{LUMO}(eV) = -e(E_{red} + 4.80) \qquad (5)$$

$$E_g(eV) = E_{LUMO} - E_{HOMO} \qquad (6)$$

Wherein E_{HOMO} and E_{LUMO} represent the energy levels of HOMO and LUMO orbitals, E_{ox} and E_{red} are the onset oxidation and reduction potentials, respectively. The E_{ox} and E_{red} values were obtained from the CVs and the related data were given in Table 1. The HOMO energy levels of all of complexes are more negative than $FADH_2$, indicating adequite driving force for the electron transfer from $FADH_2$. Herein, we have supposed the redox potential of FAD, since the value has not been studied. g-C_3N_4 has been implemented owing to its favorable energetic state of CB which acts as an electron trap for excited electrons of Ru-complex and reinforce the photogenerated charge separation within Ru-complex and, as such, enhance the incident photon-to-current efficiency. The LUMO energy levels of excited complexes have more positive potentials compared to the VB energy level of g-C_3N_4, which confirms that the electron injection is thermodynamically favorable process through the photosensitive hybrid material(Zhao et al., 2015). The energy levels of complexes and semiconductor can be seen in Table 1 and Scheme 1B.

Table 1. Spectrophotometric, electrochemical and photoelectrochemical properties of light-sensitive materials in deoxygenated DMF and MeCN

Ru-complexes semiconductor	Absorbance λ_{max} (nm)	Emmision λ_{max} (nm)	E^{ox} (V vs $Ag/AgNO_3$)	E^{red} (V vs $Ag/AgNO_3$)	E_{HOMO} (eV)	E_{LUMO} (eV)	E_g (eV)	Φ (10^{-4})	τ (ns)
Ru1	440	623	0.98	-1.68	-5.78	-3.12	2.66	24	179.4
Ru2	430 - 530	618	0.50	-1.84	-5.30	-2.96	2.34	11	6.86
Ru3	507	no band	0.41	-1.94	-5.21	-2.86	2.35	6	2.08
g-C_3N_4	385	-	1.10	no peak	E_{VB} -5.90	E_{CB} -3.16	2.74	-	-

3.2. Photoelectrocatalytic activity of the bioanode

The CVs were obtained in argon-saturated 0.1 M PBS at pH:7.0 to investigate the accessibility of Ru-complexes (Figure S5). Although, CVs of the electrode without Ru-complex displayed no redox process, the CVs of Ru-complexes modified electrodes exhibit the well-defined reversible redox processes for the two electron and two proton quinone/hydroquinone transition of the PLQ ligand. The $E_{1/2}$ values were found to be -0.01 V (Ru1), -0.025 V (Ru2) and -0.04 V (Ru3) vs. Ag/AgCl with peak-to-peak separations (ΔE_P) of 0.1 V, 0.15 V and 0.08 V, respectively. Larger ΔE_P is an indicative of slow electron transfer due to possible diffusion issues of electrolyte through the deposit. Another plausible reason is that electron tunneling distances and nanomaterial resistivity increase when the Ru-complex is embedded in the MWCNT network. The smallest ΔE_P was observed for Ru-complex 1 confirming its superiority to the other Ru-complexes for bioanode construction.

3.3. Photogenerated charge convey through the photobioanode

The electron transport process was demonstrated in Scheme 1B. At the first step, the electron transport process is initiated by photoexcitation of Ru-complex sensitizer concurrently generating the excited state of Ru-complex (Ru-complex*) and photoinduced charge separation occurs at the Ru-complexg|C_3N_4 interface. Since the energy level of Ru-complex* matches well with the CB of g-C_3N_4, photoexcited electrons flow to the underlying g-C_3N_4 layer and then to the MWCNT coated GCE. The charge recombination diminishes by forming Ru-complex radical cation (Ru-complex*$^+$). The injected electron migrates to the underlying GCE and travels through an external circuit to the biocathode, thus generating electricity. At the biocathode, molecular oxygen is reduced to water by BOx. At the second step, hole scavenging process at the photoanode by enzymatic glucose oxidation takes place. Meanwhile, the oxidized Ru-complex*$^+$ accepts an electron from $FADH_2$ finally generating the oxidized form of the mediator, FAD, with concomitant two electron transfer and Ru-complex is reduced to the ground state. FAD serves as an electron acceptor of FADGDH for the enzymatic oxidation of glucose, which regenerates $FADH_2$. FADGDH catalyzed, and redox complex mediated electron transfer is analogous to the bioanode operation of an enzymatic biofuel cell (Gross et al., 2018). However, photobioanode also converts the light energy into electricity. MWCNTs are an efficient electron collectors for the underlying

photosensitive entity, and reduces the hole/electron recombination rate(Çakıroğlu and Özacar, 2018).

Photochronoamperometric measurements were recorded in 170 mM glucose solution due to tha fact that enzymatic reaction velocity limits the electron transfer rather than glucose concentration as can be confirmed by next glucose measurements (Figure 3A). Upon visible light illumination, the GCE|MWCNT|g-C_3N_4|FADGDH photoanode at 0 V vs. Ag/AgCl in PBS shows an increment in photocurrent (ca. 0.39 μA cm^2), but GCE|MWCNT|FADGDH shows no measurable photocurrent (not shown). The photocurrent enhances 0.61 and 0.94 μA cm^2 for Ru3 and Ru2 immobilized photoelectrode, respectively. Finally, GCE|MWCNT|g-C_3N_4|Ru1|FADGDH yielded the most enhanced photocurrent of 2.5 μA cm^2 owing to its higher photon-to-current efficiency and charge convey. Therefore, the photogenerated electrons should transfer from the $FADH_2$ to Ru-complex and then semiconductor. As a rule, anodic photocurrent proportionally increases with the increasing distance between the redox potential of electron donor $FADH_2$ and the HOMO level of Ru-complex and the lowest HOMO energy level was observed for Ru-complex 1. Therefore, Ru1 is more prone to reduction by $FADH_2$ and thus increased photocurrent intensity. The biocatalysis of glucose led to the transfer of enzymatic electrons to g-C_3N_4 and distinctly improve the photocurrent generation. The photocurrent-wavelength curve of the GCE|MWCNT|g-C_3N_4|Ru1 yielded the maximum photocurrent wavelength at 462 nm (Figure S6), which is near to the absorbance wavelength of Ru1 (Figure 2A).

As for the potential-photocurrent profile of GCE|MWCNT|g-C_3N_4|Ru1, measurements under illumination with glucose demonstrated the anodic photocurrents throught the whole range between -0.5 V and 0.4 V vs Ag/AgCl. In Figure 3B, the pronounced anodic photocurrents were observed at -0.4 and 0.2 V in the presence of 170 mM glucose and slightly enhanced photocurrents were observed at positive potentials. No photocurrents could be measured in the dark. Light-driven glucose oxidation at quite negative potentials was achieved only by Riedel *et al* (Riedel et al., 2018) by using PQQGDH immobilized osmium-complex-containing polymer and PbS QDs coated TiO_2 inverse opal photoelectrode. The photobioanode exhibited the maximum photocurrent density of 6.78 μA cm^{-2} at 0.2 V vs Ag/AgCl at pH:7. According to the literature, g-C_3N_4 on fluorine-doped tin oxide (FTO) coated glass electrode generated a photocurrent of 0.2 μA cm^2 at 0.6 V vs. SCE (>420 nm, 200 W Xe lamp, 0.2 M Na_2SO_4) (Xie et al., 2016). g-C_3N_4/CNT on FTO electrode yielded a photoresponse of 1.8 μA cm^{-2} at 0 V vs. SCE (0.5 M Na_2SO_4) (Miao et al., 2017), confirming the electron collecting feature of

CNT. g-C_3N_4/Ag/MoS_2 coated FTO produced a photocurrent of 3.12 µA cm^{-2} at 0.5 V vs. Ag/AgCl (0.5 M Na_2SO_4, light intensity: 100 mW cm^{-2}) (Hu et al., 2015). The improved current can be attributed to the increased excited electrons after combining different semiconductors and excellent electron transfer through Ag. g-C_3N_4 quantum dots/TiO_2 nanotube arrays exhibited significantly improved photocurrent of 1.34 mA cm^{-2} at 0.3 V vs. Ag/AgCl (0.1 M Na_2SO_4 (pH 6.0), light intensity: 100 mW cm^{-2}) (Su et al., 2016) probably due to the combination of semiconductors, enhanced surface area of TiO_2 nanotube arrays and utilization of larger light intensity. In this study, we suppose that MWCNT increases electron collection coming from g-C_3N_4 layer with a cascade electron transfer, enhances the conductivity within the electrode material. The photosensitive material reinforced the electron transfer and the sensitization led to efficient light energy harnessing by generating photocurrent.

Therefore, the present photoanode was rationally fabricated with an electron collecting property and enhanced surface area.

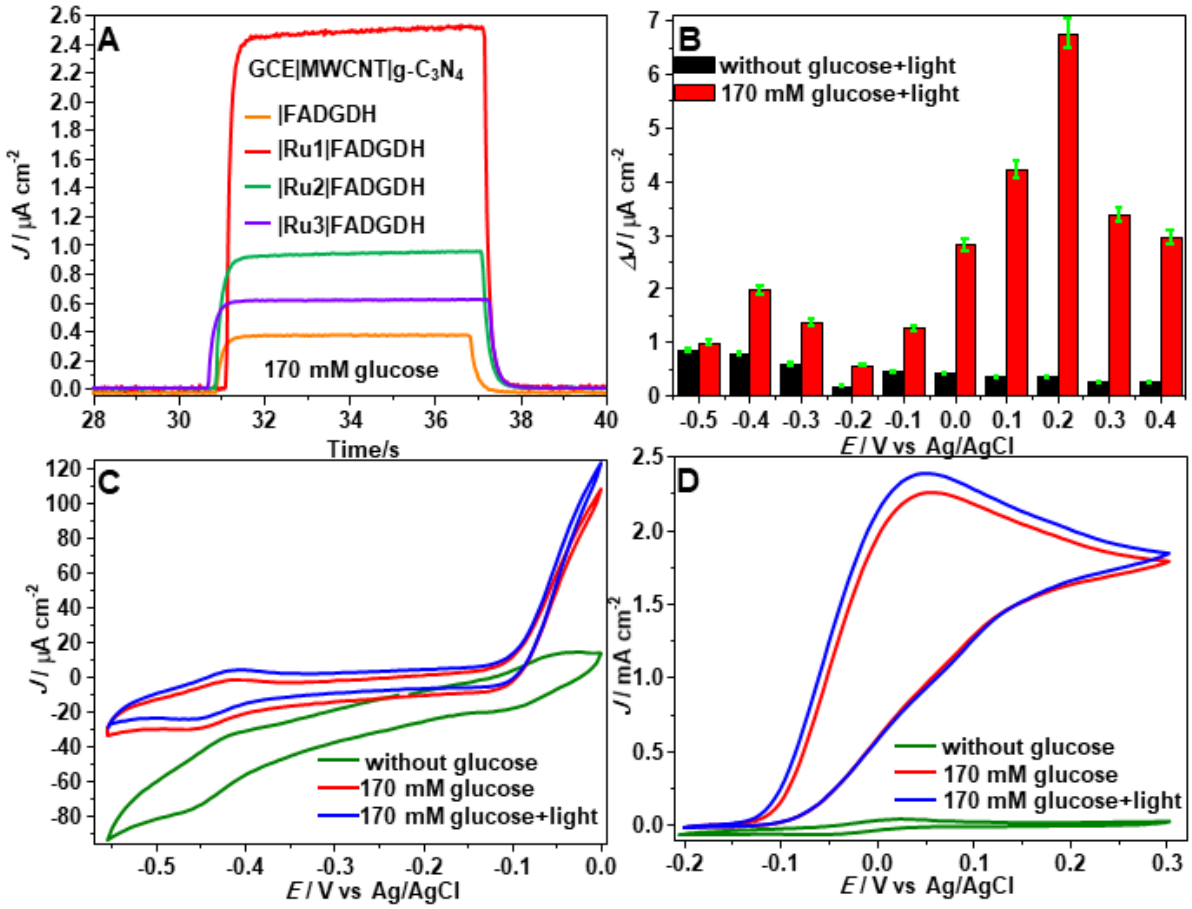

Figure 3. Photochronoamperometric measurement of the bioanodes modified with g-C_3N_4 (orange bar), Ru1 (red bar), Ru2 (green bar), and Ru3 (purple bar) with 170 mM glucose (poised at E = 0 V vs Ag/AgCl, visible light is switched on from 10 to 20 s; 11.2 mW cm^{-2})

(A); and at different potantials in the absence (black bar), and with 170 mM glucose under illumination (red bar) in argon saturated 0.1 M PBS pH 7 (B) (The data are the average of three replicates with error bars representing standard deviation); CVs of the GCE|MWCNT|g-C_3N_4|Ru1|FADGDH electrode in the absence (green curve), presence (red curve) of 170 mM glucose, and under illumination (blue curve) in argon saturated 0.1 M PBS, pH 7 (scan rate, 2 mV s^{-1}) (C) and (D).

The CVs evidently confirms an increment in glucose oxidation current to some extent under irradiation in argon purged PBS containing 170 mM glucose (Figure 3C, D, Figure S7 and Figure 4A). To rule out the any photocurrent generation induced by molecular gases, the buffer was purged with inert gas. The onset potential values is of great importance in BFC applications to achieve superior performance. Well-defined sigmoidal curves were observed with a low onset potential of E_{onset} = −0.13 ± 0.05 V vs Ag/AgCl, which is desirably low for a bioanode and indicates mediated electron transfer through PLQ-Ru-complex. The onset potential is found to be similar to those obtained using 1,10-phenanthroline-5,6-dione-Ru-complex containing polymer with FADGDH from *Aspergillus terreus* (E_{onset} = −0.1 V vs Ag/AgCl at pH 7)(Sakuta et al., 2015) and 1,4-naphthoquinone appended redox polymer with FADGDH from *Aspergillus sp.* (E_{onset} = −0.13 V vs Ag/AgCl at pH 6) (Hou et al., 2016) and phenanthrolinequinone (phendione) tailored Ru-complex with fungal FADGDH (E_{onset} = −0.1 V vs Ag/AgCl at pH 7)(Fritea et al., 2019). The onset potential is also more negative than those found using poly(1-vinylimidazole)-tethered Os(2,2′-bipyridine)$_2$Cl-modified electrode with FADGDH from *Aspergillus terreus* (0.1 V vs Ag/AgCl)(Murata et al., 2014), osmium complex functionalized polymer coated electrode with FADGDH from *Aspergillus sp.* (E_{onset} = 0.2 V vs Ag/AgCl)(Ó Conghaile et al., 2013), and ferrocene gifted redox hydrogel modified electrode with FADGDH from *Aspergillus sp.* (E_{onset} of 0.05 V vs. SCE)(Ross D. Milton et al., 2015). Therefore, Ru-PLQ-complex is an attractive mediator for bioelectrocatalysis of glucose compared to osmium and ferrocene containing mediators. Under illumination and in unstirred buffer, the subtantial glucose oxidation current of 2.39 ± 0.54 mA cm^{-2} at 0.05 V vs Ag/AgCl exceeds the current obtained without illumination (2.25 ± 0.45 mA cm^{-2}) due to the PEC process. In contrast, CVs recorded in the absence of glucose reveal a negligible current density which gives a hint for the efficient construction of the bioanode toward glucose biocatalysis. Also, the FADGDH immobilized electrode without Ru-complex displayed low glucose oxidation currents in the presence of glucose confirming that both Ru-complex and FADGDH are needed to provide the biocatalytic activity (Figure S4). All in all, bioanodes

with immobilized FADGDH outperform the electrodes with glucose oxidase and other glucose dehydrogenases, and FADGDH has yielded high current densities up 5.38 ± 0.54 mA cm^{-2} at 0.15 V(Gross et al., 2017).

The V_{OC} of the biofuel cell can be boosted by using a biocathode with a large reduction potential (Xiao et al., 2019). BOx from Myrothecium verrucaria (Mv) was immobilized for the reduction of O_2 to H_2O at the biocathode part. BOx is widely used in the BFCs owing to its higher biocatalytic activity and less sensitivity to chloride ions at physiological conditions(Xiao et al., 2019). DET is attained by favorable orientation of BOx during immobilization. Figure 4B shows the CVs recorded in argon and oxygen saturated buffer by using biocathode. In the oxygenated buffer, biocathode exhibited steeper cathodic catalytic wave with an onset potential of 0.54 V vs Ag/AgCl and compatible with single-proton single-electron DET during oxygen reduction by BOx. The half-wave potential of 0.45 V vs. Ag/AgCl is close to the redox potential of the T1 copper active site of multicopper oxidase ($E_{1/2}$(T1) = 0.48 V vs SCE at pH 7.0) (Bourourou et al., 2014) and close to the thermodynamic O_2 reduction potential (0.572 V vs SCE at pH 7.0) (Gross et al., 2017). The maximum oxygen reduction current of 0.43 ± 0.14 mA cm^{-2} is larger than that obtained on engineered BOx immobilized GCE/MWCNT electrode (16 μA cm^{-2}) (Al-Lolage et al., 2019), and comparable to that achieved on BOx immobilized MWCNTs coated biocathode by using anthracene modification to orientate BOx (500 μA cm^{-2}) (Aquino Neto et al., 2016), and MWCNT modified Toray paper electrode (~350 μA cm^{-2})(Ramasamy et al., 2010). The close contact of BOx to the MWCNTs enabled us satisfying cathodic current.

3.4. Photoelectrochemical biofuel cell studies

The schematic illustration of PBFCs is shown in Figure 1B. A PEC flow cell setup was applied to investigate the power characteristics of the PBFC assembly by inserting the as-prepared photobianode and biocathode (0.071 cm^2) in parallel with a distance of 1.5 mm. The short distance between the electrodes diminishes the electrolyte resistance and the current loss. At the bioanode, phosphate buffer containing different glucose concentrations was pushed into the cell compartment. At the biocathode, oxygenated PBS was flown through external pumps at room temperature. The light source was vertically placed at the front of the bioanode. The buffer flows were adjusted qualitatively and moderately to attain reproducible results. Thus, a membraneless glucose/O_2 PBFCs was constructed.

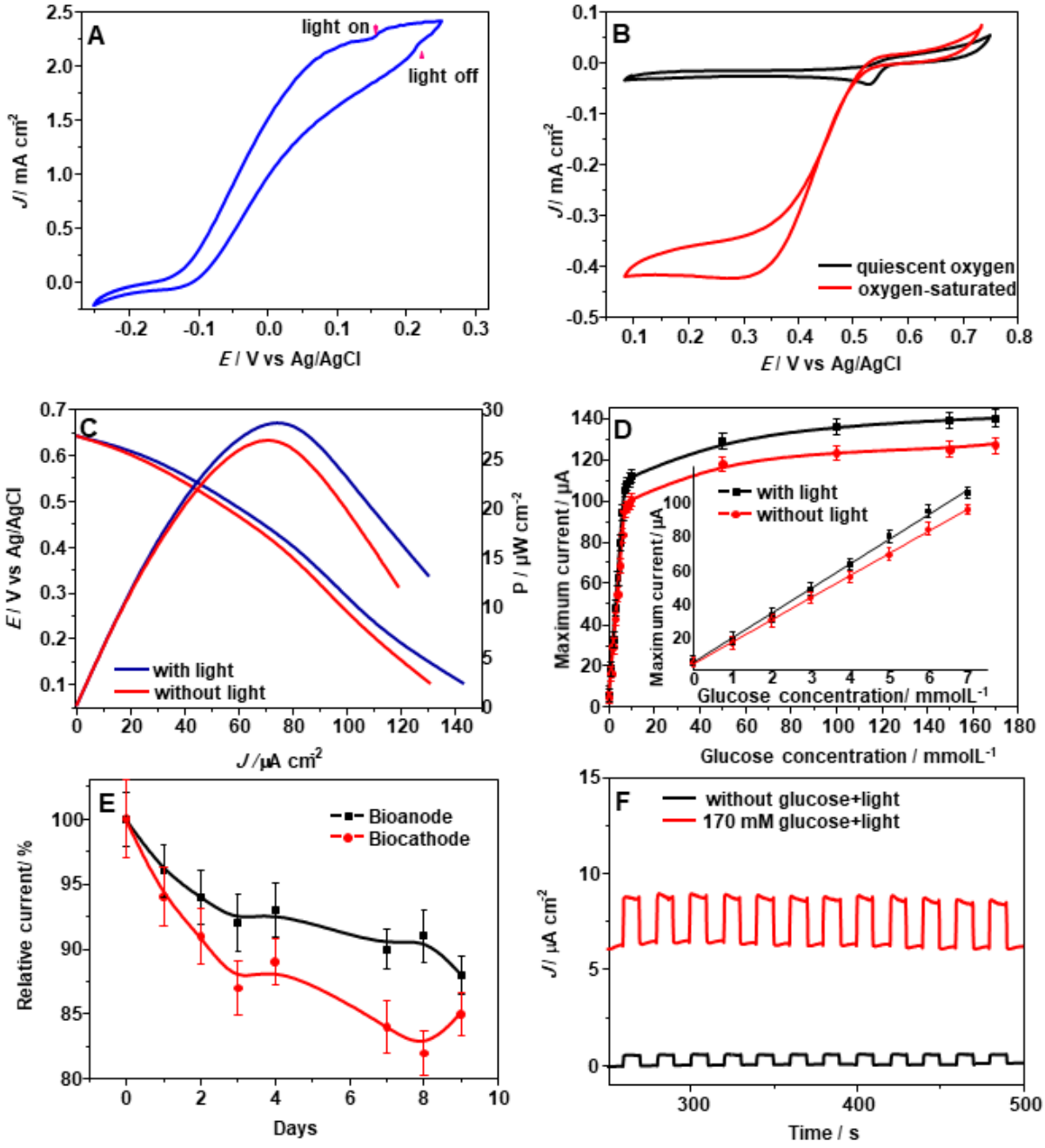

Figure 4. CV of the GCE|MWCNT|g-C_3N_4|Ru1|FADGDH electrode in the presence of 170 mM glucose, and under on-off illumination in argon saturated 0.1 M PBS, pH 7 (scan rate: 2 mV s^{-1}) (A); CVs of the GCE|f-MWCNT|BOx under argon, and oxygen-saturated 0.1 M PBS pH 7 (B); Power density and polarization curves for PBFC in 0.1 M PBS (pH 7.0) containing oxygen-saturated 170 mM glucose upon visible light illumination; scan rate: 2 mV s^{-1} (C); the dependence of the oxidation current on varying glucose concentrations (D); The storage stability of the bioanode and biocathode recorded for 9 days (E); The photocurrent cycle of photobioanode with the light on and off operating at 0.2 V (F).

BFC studies were carried out by obtaining polarization curves from the V_{OC} to 0.1 V by connecting the bioanode to the counter and reference leads, and the cathode to the working lead. Figure 4C shows the polarization and power density curves of the biofuel cells. According to Figure 4C, PBFC delivers an V_{OC} of 0.64 V and the maximum power density (P_{max}) of 28.4 ± 0.7 μW cm^2 at 0.42 V, which is larger than that obtained without illumination (26.7 ± 0.4 μW cm^2) due to the conversion of both, light energy and chemical energy to produce electricity. The V_{OC} is close to the calculated maximum voltage of 0.67 V according to the half-cell polarization studies. Maximum power output is comparable to that achieved in FADGDH immobilized redox polymer and PbS QDs deposited TiO_2 inverse opal electrode (31.3 ± 2.7 μW cm^{-2} at −287 ± 80 mV vs Ag/AgCl)(Riedel et al., 2018), and NAD-dependent glucose dehydrogenase (GDH) incorporated porphyrin sensitized meso-TiO_2 electrode (33.94 μW cm^{-2} at 0.45 V)(Wang et al., 2012). Also, the obtained power output is larger than that obtained on GDH incorporated porphyrin sensitized SnO_2 electrode (19 μW cm^{-2} at 0.45 V)(de la Garza et al., 2003), and glucose oxidase immobilized tetrathiafulvalene modified mesoporous carbon electrode (23.65 μW cm^{-2})(Zhang et al., 2014).

The maximum current output vs. glucose concentration graphs displayed a Michaelis-Menten kinetics (Figure 4D). According to the calibration curves derived from the linear part of the graphs (Figure 4D inset), the regression equation was calculated as I (μA) e=14.5$C_{glucose}$ (mM) + 4.87 (R^2 = 0.998) under illumination. The sensitivities were estimated as 13.1 μA cm^{-2} and 14.5 μA cm^{-2} without and with illumination, respectively. The limit of detection (LOD) based on 3x(standard deviation of 10 blank measurements/sensitivity) was estimated to be 15 μM and the limit of quantification based on 10x(standard deviation of 10 blank measurements/sensitivity) was estimated to be 50 μM under illumination.

The PBFC performance can be determined by η, J_{SC}, V_{OC} and fill factor (FF) values. The FF and light energy conversion efficiency (η) can be estimated by Eqs. (7) and (8)(Wang et al., 2012).

$$\eta = \frac{Jsc\ xVoc\ x\ FF}{Pin} \qquad (7)$$

$$FF = \frac{Jm\ x\ Vm}{Jsc\ xVoc} \qquad (8)$$

Wherein J_m and V_m are the maximum current and potential values, respectively and J_{SC} is the short current density. P_{in} is the light intensity (11.2 mW cm^2). FF is calculated to be 0.14 ± 0.05, and η was estimated as 1.152.

The operational stabilities of the bioelectrodes were also assessed at a mild fixed potential of 0.2 V by recording the current in optima buffer solutions over 9 days (Figure 4E). At the end, 88% and 85% of their initial currents remained for bioanode and biocathode, respectively. The plots indicates that the photobioanode is evidently more stable than the biocathode. The enhanced stability is due to the enhanced physical enzyme immobilization into the MWCNT matrix, reduced toxicity of hybrid material toward the enzyme and Nafion coating. The robust short-term operational stability is favorable for the commercial production of a single-compartment PBFC. The obtained bioanode and biocathode stabilities were found to be comparable to other FADGDH based electrodes(Hiratsuka et al., 2019), and superior to those achieved with GOx based glucose/oxygen BFCs(Zebda et al., 2011).

The stability of the photocurrent generation was tested under on-off light cycles (Figure 4F). The photocurrent remained nearly constant after 20 cycles, supporting the high stability of the immobilized entities due to the utilization of π−π stacking interactions.

CONCLUSIONS

Herein, we represent a proof-of-concept advance in dual-directional energy conversion in BFCs. The Ru-complex embedded g-C_3N_4 and MWCNT hybrid material acted as a platform to immobilize FADGDH for the visible light assisted glucose oxidation at the bioanode, and BOx was employed at the biocathode. Thus, a membraneless and visible light assisted glucose/air PBFC was assembled. An enhancement in glucose oxidation current could be ascribed to the high surface area, good electrical contacting of FADGDH to the light-sensitive hybrid material and efficient light energy utilization. The BFC revealed good operational stability and fast and stable response, which prove its feasibility for the mass production of PBFCs to determine glucose on self-powered mode. The higher P_{max} for BFC under visible light could be attributed to efficient light utilization and the PBFC couples the photogenerated charge separation to the biocatalytic glucose oxidation by FADGDH. The irradiation of the photobioanode enhanced the overall performance of the PBFC. We suppose that different photosensitive materials and robust architectures with intimate contact between the

components will yield larger V_{OC} values and semiconducting systems with high photon-to-current conversion efficiencies will generate unprecedented photocurrents and power outputs. PBFCs will extend the insight beyond the conventional BFCs.

Acknowledgments

The French National Centre for Scientific Research and Turkish Council of Higher Education (YÖK YUDAB) are acknowledged for the research budget. B. Çakıroğlu would like to thank Dr. Jules L. Hammond and Dr. Deborah Brazzolotto for their valuable contributions. The authors also gratefully acknowledge the support from the platform Chimie NanoBio ICMG FR 2607 (PCN-ICMG and PMIEL), from the LabEx ARCANE (ANR-11-LABX-0003-01 and CBH-EUR-GS, ANR-17-EURE-0003), and from the Institut Carnot PolyNat (CARN 0007-01). We are very grateful to Christine Lancelon Pin for assistance with SEM imaging.

References

Akkaya, B., Çakıroğlu, B., Özacar, M., 2018. ACS Sustainable Chemistry & Engineering 6, 3805–3814.

Al-Lolage, F.A., Bartlett, P.N., Gounel, S., Staigre, P., Mano, N., 2019. ACS Catalysis 9, 2068–2078.

Aquino Neto, S., Milton, R.D., Hickey, D.P., De Andrade, A.R., Minteer, S.D., 2016. Journal of Power Sources 324, 208–214.

Bourourou, M., Elouarzaki, K., Holzinger, M., Agnès, C., Le Goff, A., Reverdy-Bruas, N., Chaussy, D., Party, M., Maaref, A., Cosnier, S., 2014. Chemical Science 5, 2885–2888.

Çakıroğlu, B., Özacar, M., 2019. Biosensors and Bioelectronics 141, 111385.

Çakıroğlu, B., Özacar, M., 2018. Biosensors and Bioelectronics 119, 34–41.

Caspar, J. V, Meyer, T.J., 1983. Journal of the American Chemical Society 105, 5583–5590.

Cevallos-Vallejo, A., Vonlanthen, M., Porcu, P., Ruiu, A., Rivera, E., 2017. Tetrahedron Letters 58, 1319–1323.

Cheng, J., Han, Y., Deng, L., Guo, S., 2014. Analytical Chemistry 86, 11782–11788.

de la Garza, L., Jeong, G., Liddell, P.A., Sotomura, T., Moore, T.A., Moore, A.L., Gust, D.,

2003. The Journal of Physical Chemistry B 107, 10252–10260.

Dong, Y., Wang, Q., Wu, H., Chen, Y., Lu, C.H., Chi, Y., Yang, H.H., 2016. Small 12, 5376–5393.

Elouarzaki, K., Holzinger, M., Goff, A. Le, Thery, J., Marksae, R.S., Cosnier, S., 2016. Journal of Materials Chemistry A 4, 10635–10640.

Eswaran, R., Kalayar, S., Paulpandian, M.M., Seenivasan, R., 2014. Journal of Fluorescence 24, 875–884.

Fritea, L., Gross, A.J., Reuillard, B., Gorgy, K., Cosnier, S., Le Goff, A., 2019. ChemElectroChem 6, 3621–3626.

Gai, P., Kong, X., Zhang, S., Song, P., Li, F., 2020. Chem. Commun. 56, 7116–7119.

Goss, A. C., D. Abruna, H., 1985. Inorganic Chemistry 24, 4263–4267.

Gross, A.J., Chen, X., Giroud, F., Abreu, C., Le Goff, A., Holzinger, M., Cosnier, S., 2017. ACS Catalysis 7, 4408–4416.

Gross, A.J., Holzinger, M., Cosnier, S., 2018. Energy and Environmental Science 11, 1670–1687.

Hiratsuka, A., Iwasa, H., Uzawa, H., Suzuki, A., Muguruma, H., 2019. ACS Omega 4, 5776–5783.

Holzinger, M., Le Goff, A., Cosnier, S., 2012. Electrochimica Acta. pp. 179–190.

Hou, C., Lang, Q., Liu, A., 2016. Electrochimica Acta 211, 663–670.

Hu, S.W., Yang, L.W., Tian, Y., Wei, X.L., Ding, J.W., Zhong, J.X., Chu, P.K., 2015. Applied Catalysis B: Environmental 163, 611–622.

Jeerapan, I., Sempionatto, J.R., Pavinatto, A., You, J.-M., Wang, J., 2016. J. Mater. Chem. A 4, 18342–18353.

Kumar, A., Kumar, P., Borkar, R., Bansiwal, A., Labhsetwar, N., Jain, S.L., 2017. Carbon 123, 371–379.

Lalaoui, N., de Poulpiquet, A., Haddad, R., Le Goff, A., Holzinger, M., Gounel, S., Mermoux, M., Infossi, P., Mano, N., Lojou, E., Cosnier, S., 2015. Chem. Commun. 51, 7447–7450.

Miao, H., Zhang, G., Hu, X., Mu, J., Han, T., 2017. Journal of Alloys and Compounds 690, 669–676.

Milton, R.D., Giroud, F., Thumser, A.E., Minteer, S.D., Slade, R.C.T., 2013. Phys. Chem. Chem. Phys. 15, 19371–19379.

Milton, Ross D, Hickey, D.P., Abdellaoui, S., Lim, K., Wu, F., Tan, B., Minteer, S.D., 2015. Chemical Science 6, 4867–4875.

Milton, Ross D., Lim, K., Hickey, D.P., Minteer, S.D., 2015. Bioelectrochemistry 106, 56–63.

Moehlenbrock, M.J., Minteer, S.D., 2008. Chem. Soc. Rev. 37, 1188–1196.

Monsalve, K., Roger, M., Gutierrez-Sanchez, C., Ilbert, M., Nitsche, S., Byrne-Kodjabachian, D., Marchi, V., Lojou, E., 2015. Bioelectrochemistry 106, 47–55.

Murata, K., Akatsuka, W., Sadakane, T., Matsunaga, A., Tsujimura, S., 2014. Electrochimica Acta 136, 537–541.

Ó Conghaile, P., Pöller, S., MacAodha, D., Schuhmann, W., Leech, D., 2013. Biosensors and Bioelectronics 43, 30–37.

Opperman, K.A., Mecklenburg, S.L., Meyer, T.J., 1994. Inorganic Chemistry 33, 5295–5301.

Ramasamy, R.P., Luckarift, H.R., Ivnitski, D.M., Atanassov, P.B., Johnson, G.R., 2010. Chem. Commun. 46, 6045–6047.

Rasmussen, M., Abdellaoui, S., Minteer, S.D., 2016. Biosensors and Bioelectronics 76, 91–102.

Reuillard, B., Le Goff, A., Cosnier, S., 2014. Chemical Communications 50, 11731–11734.

Riedel, M., Parak, W.J., Ruff, A., Schuhmann, W., Lisdat, F., 2018. ACS Catalysis 8, 5212–5220.

Sakuta, R., Takeda, K., Ishida, T., Igarashi, K., Samejima, M., Nakamura, N., Ohno, H., 2015.

Electrochemistry Communications 56, 75–78.

Su, J., Zhu, L., Chen, G., 2016. Applied Catalysis B, Environmental, 186, 127–135.

Wang, K., Yang, J., Feng, L., Zhang, Y., Liang, L., Xing, W., Liu, C., 2012. Biosensors and Bioelectronics 32, 177–182.

Xiao, X., Xia, H.Q., Wu, R., Bai, L., Yan, L., Magner, E., Cosnier, S., Lojou, E., Zhu, Z., Liu, A., 2019. Chemical Reviews 119, 9509–9558.

Xie, X., Fan, X., Huang, X., Wang, T., He, J., 2016. RSC Advances 6, 9916–9922.

Yang, J., Hu, D., Zhang, X., Wang, K., Wang, B., Sun, B., Qiu, Z., 2014. Journal of Power Sources 267, 617–621.

Yu, Y., Han, Y., Xu, M., Zhang, L., Dong, S., 2016a. Nanoscale 8, 9004–9008.

Yu, Y., Xu, M., Dong, S., 2016b. Chemical Communications 52, 6716–6719.

Zebda, A., Gondran, C., Le Goff, A., Holzinger, M., Cinquin, P., Cosnier, S., 2011. Nature Communications 2.

Zhang, G., Lan, Z.A., Wang, X., 2017. Chemical Science 8, 5261–5274.

Zhang, L., Bai, L., Xu, M., Han, L., Dong, S., 2015. Nano Energy 11, 48–55.

Zhang, L., Xu, Z., Lou, B., Han, L., Zhang, X., Dong, S., 2014. ChemSusChem 7, 2427–2431.

Zhang, N., Ruan, Y.F., Zhang, L. Bin, Zhao, W.W., Xu, J.J., Chen, H.Y., 2018. Analytical Chemistry 90, 2341–2347.

Zhao, J., Wang, X., Xu, Z., Loo, J.S.C., 2014. Journal of Materials Chemistry A 2, 15228–15233.

Zhao, W.-W., Xu, J.-J., Chen, H.-Y., 2015. Chem. Soc. Rev. 44, 729–741.